Duration of Super-Emitting Oil & Gas Methane Sources

Daniel H. Cusworth[1,*], Daniel M. Bon[1], Daniel J. Varon[2], Alana K. Ayasse[1], Gregory P. Asner[3], Joseph Heckler[3], Evan D. Sherwin[4], Sebastien C. Biraud[4], and Riley M. Duren[1]

[1]Carbon Mapper, Pasadena, CA, USA

[2]School of Engineering and Applied Sciences, Harvard University, Cambridge, MA, USA

[3]Center for Global Discovery and Conservation Science, Arizona State University, Tempe, AZ, USA

[4]Climate Sciences Department, Lawrence Berkeley National Laboratory, Berkeley, CA, USA

*Corresponding author. Email: dan@carbonmapper.org

Keywords: methane, super-emitters, emission duration, imaging spectroscopy

This is a non-peer-reviewed preprint submitted to EarthArXiv.

Abstract

The duration of super-emitting events in oil & gas basins remains poorly understood but is key for informing reporting programs and mitigation strategies. Carbon Mapper conducted intensive aerial surveys from April 30 to May 17, 2024, over the New Mexico portion of the Permian Basin to estimate super-emitter durations directly from observations, covering 276,000 wells, 1100 compressor stations, 175 gas processing plants, and 27,000 km of pipeline. During the campaign, we detected over 500 super-emitting sources and surveyed over 300 of these sources repeatedly. Over the repeatedly surveyed region, we quantified total emissions by integrating individual events with observationally constrained event durations (5.98 -14.7 Gg CH_4) and compared this estimate to the total emissions derived from basin average snapshots (12.7 ± 0.92 Gg CH_4). We show that this emissions gap can plausibly be reconciled through assumptions on missed detections, particularly given the strong relationship between characteristic event duration, detection frequency, and diurnal variability. We attribute each event to specific infrastructure types and find that emissions from compressors were detected most frequently and generally exhibit long emission durations. A small subset of sources (18 total), mostly compressors, persistently emitted throughout the entire campaign, representing a near-term opportunity for mitigation. Sustained and frequent wide-area monitoring is crucial for capturing rare, but significant super-emitter events that, together with other sources, drive basin-level variability and emission intensity.

Introduction

Super-emitting methane sources (>100 kg CH_4 h^{-1})[1] disproportionately contribute to total emissions in many large oil & gas producing basins[2-4], meaning that a relatively small fraction of infrastructure (~0.5-1%) may represent a large contribution to total emissions[5]. This outsized effect from super-emitters therefore in many cases drives basin-level variability and intensity[6]. Super-emissions result from a variety of processes across the oil & gas supply chain, including what are commonly thought to be short duration known process events (e.g., liquids unloadings, compressor blowdowns, other pressure releases) or process aberrations (e.g., faulty equipment, leaking infrastructure, other operational issues).

The contribution of super-emitters to net emissions remains difficult to parametrize in traditional bottom-up modeling approaches that quantify emissions using emission factors and activity data, due to several key challenges. First, because super-emitters are rare relative to total infrastructure in a basin, robustly constraining the probability distributions of these events requires surveying a significant amount of representative infrastructure: identifying and characterizing events occurring at a rate of one in one hundred or one in one thousand necessitates tens to hundreds of thousands of site-level observations. Ground-based measurement surveys, that historically provides the foundation for emission factors in bottom-up inventories[7], are limited in spatial coverage, collectively. Multiple measurement campaigns have resulted in only a few thousand site-level observations across multiple basins[8]. Second, most ground-based technologies have not been rigorously validated for quantification at high emission rates. In one blinded controlled-release study, fixed ground-based sensors severely underestimated super-emitter sized events, likely due to the challenges in quantifying and accounting for transport dynamics and the vertical structure of methane plumes[9]. These two factors independently can have the effect of reducing the influence of large emission sources on net emissions when incorporated into traditional bottom-up inventories[8].

Improved incorporation of facility-scale atmospheric measurements into accounting frameworks is critical for understanding the contribution and dynamics of emissions from both super-emitting and non-super-emitting sources. Measurement informed inventories have been successfully prototyped in previous studies[2,10,11], and provide an empirical and statistical mechanism to reconcile the bottom-up and top-down emission estimates at the basin level. A key assumption in these analyses is that population statistics from a single scan of a basin provide generalizable information about the prevalence and contribution of super-emitters. Aerial measurement technologies, such as fixed-wing LiDAR[12] and passive remote sensing[13-15] have been pivotal to these studies, enabling efficient observation of the thousands to hundreds of thousands of sites needed to understand the dynamics of super-emitters. To date, aerial quantification shows little to no systematic bias at high emission rates when evaluated against blinded controlled releases[16].

Though useful for application of basin-level inventory accounting, such approaches provide limited information regarding the true intermittency and duration of emission events at individual sites. This is of great importance for reporting programs such as the U.S. Greenhouse Gas Reporting Program (GHGRP), which requires operators to report methane emissions from large sources to the U.S. Environmental Protection Agency (EPA). In 2024, EPA updated the oil & gas reporting protocols of the GHGRP (Subpart W), requiring the reporting of "other large releases" above 100 kg h^{-1} (i.e., super-emitters). Similarly, the United Nations Oil and Gas Methane Partnership 2.0 (OGMP; https://www.ogmpartnership.com) provides a measurement-based framework for oil & gas companies to report and track their emissions through direct measurement at facility scales, with the goal of improving accountability and progress towards emission mitigation targets. In this framework, understanding the intermittency and duration of emissions is essential for accurate accounting and reconciliation.

Given the complexity of oil & gas systems, relatively little public data exists characterizing representative emission durations across general classes of operations. One study, performed at two midstream compressor stations in New York using continuous emissions monitoring system (CEMS) observations and operators reports, estimated average super-emitter durations of 30 minutes, with a minority but significant number of events lasting longer than 5 hours[18]. However, super-emitters events span various infrastructure types and supply-chain segments (e.g., tanks, flares, pipelines), and are operator dependent. A separate study[14] based on broad aircraft surveys over a six-week period found a class of persistently super-emitting infrastructure in the Permian Basin, associated with multiple infrastructure types, indicating that some event may have durations longer than sub-hour.

In this study, we conducted intensive aerial surveys over a three-week period between April and May 2024 on the New Mexico side of the Permian Basin. The campaign was specifically designed to address questions related to both the intensity and duration of super-emitters across all infrastructure and supply chain categories within the domain. Thousands of infrastructure elements were surveyed daily, often multiple times per day, and over multiple days. We identified hundreds of unique super-emitter events, estimated their durations based purely from observations, and attributed each event to specific infrastructure using high-resolution visible imagery and geographic information system (GIS) datasets. We then compared the sub-basin level emission estimate to an emission estimate derived through integration of individual events, based on their calculated event durations. Our findings reveal that a small but significant fraction of super-emitter events were persistent throughout the campaign, highlighting the potential for substantial near-term methane mitigation.

Results

Carbon Mapper conducted an airborne campaign with the Global Airborne Observatory (GAO; https://asnerlab.org/projects/global-airborne-observatory/) over the New Mexico (NM) side of the Permian Basin between April 30 – May 17, 2024 (Figure 1). The survey was designed for two primary objectives: (1) to cover the vast majority of NM oil & gas infrastructure and production at least once to estimate basin-level emissions from super-emitters (referred to here as the "Full Region"), and (2) to focus on high-production regions with multiple revisits over subsections of the basin to quantify the duration of unique super-emitter events. These intensive areas of interest were subdivided into two regions, the "West Box" and the "East Box."

The Full Region covers 12,000 km^2 which according to the Rextag oil & gas infrastructure database (https://www.rextag.com), includes 67,000 wells, 98% of NM Permian oil Production, and 98% of NM Permian gas production, along with 295 compressor stations and 45 gas processing plants. During the campaign, the Full Region was mapped wall-to-wall, meaning complete coverage of all oil & gas infrastructure, including 17,000 miles of gathering and transmission pipelines. The West Box covers 1,200 km^2, including 6400 wells, 16% of NM Permian oil production, and 22% of NM Permian gas production. It was mapped entirely multiple times per day on May 1, 13, and 15, with partial coverage on 4 additional flight days. The East Box also covers 1,200 km^2, including 9,200 wells, 35% of NM Permian oil production, and 42% of NM Permian gas production. It was mapped entirely multiple times per day on April 30 and May 14, with partial coverage on 4 additional flight days. Together, we estimate over 200,000 site level observations were made during the course of the campaign, when accounting for multiple survey revisits.

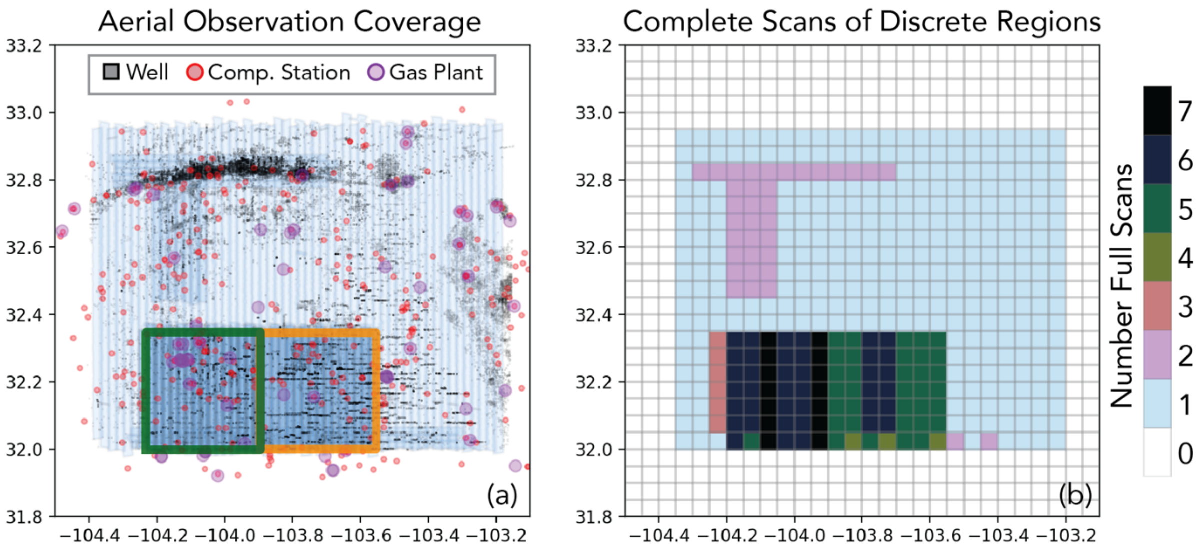

Figure 1. Observation coverage of aerial survey. (Panel a) Flight outlines of observed areas by Carbon Mapper, with Rextag reported well-sites (black squares), compressor stations (red dots), and gas plants (purple dots) overlaid. The green and orange square polygons represent areas of high production and intensive aerial surveys. (Panel b) Number of complete observational revisits across discrete 0.05 × 0.05° regions within the basin.

Carbon Mapper processes GAO radiance to identify, geolocate, and quantify large methane emission sources at sub-facility scales. These algorithms have been rigorously tested through blinded controlled release experiments, with releases ranging from 5.0 to 1500 kg h^{-1} (El Abbadi et al., 2024). The 90% probability of detection, hereafter referred to as detection limit (DL), in these controlled environments ranges between 10-45 kg per h^{-1}[19]. Alternatively, assuming a power-law distribution of oil & gas emissions in a basin[12,13], one can estimate the DL from the data by identifying the emission level at which the frequency of detections diverges from a power-law distribution. During the course of the campaign, 1,380 unique plumes were detected, and their frequency distribution suggests a DL between 70-150 kg h^{-1} (Details provided in the Supporting Information (SI), Section S1). Therefore, for the purpose of this study, we assume near-full detection sensitivity to the super-emitter class (>100 kg h^{-1}) of emissions.

Basin-level emission estimate

Figure 2a shows the locations of methane detections. To aggregate these detections into a domain-level super-emitter emission estimate (here, the NM portion of the Permian Basin), we must account for uneven temporal sampling across domain. This is done by dividing the entire survey domain into discrete 0.05° × 0.05° (≈5 × 5 km^2) grid cells and summing detected emissions per complete observational scan of each grid cell. For example, if a grid cell was surveyed in its entirety five times, there would be five independent emission estimates ("sums" of plumes) for that grid cell. In cases where an emission source was observed twice in rapid succession due to overlaps in airborne image acquisition during a single scan, only the first source observation of that source is included in the scan's emission total.

We then derive a campaign-average emission rate for each grid cell by averaging all independent emission estimates for that grid cell. Applying this across all grid cells produces a heatmap of super-emissions within the surveyed areas (Figure 2b). Uncertainties for each grid cell are calculated by first summing individual plume emission uncertainties within a single scan, then adding in quadrature the uncertainties across all scans for that grid cell. We estimate regional emissions (e.g., the Full Region) by summing mean emissions for all relevant grid cells that pertain to that domain, with uncertainties combined in quadrature. Using this method, we estimate 0.65 ± 0.06 Tg a^{-1} for the Full Region and 0.27 ± 0.02 Tg a^{-1} for the combined West + East Boxes (hereafter referred to as the "Intensive Box"). A sensitivity analysis of grid cell resolution and alternative emission quantification procedures is described in the SI (Section S2). We compare regional super-emitter estimates to total CH_4 emission fluxes derived from satellite observations by the TROPOspheric Monitoring Instrument (TROPOMI) onboard the Sentinel-5p satellite[20]. We use the Integrated Methane Inversion (IMI) system, previously applied to the Permian Basin[21,22] (Methods), to relate coarse (5.5 × 7 km^2) atmospheric concentration datasets retrieved from TROPOMI to net emission fluxes at 0.25° × 0.3125° (≈25 × 25 km^2) resolution through inverse atmospheric transport modeling regularized by a Bayesian prior emission estimate (Methods). Assimilating TROPOMI observations during the aircraft campaign period (Figure 4c), we find the total methane flux from this region of the Permian to be 1.28 ± 0.31 Tg a^{-1}, where the reported uncertainty here represents the one-sigma variability in weekly TROPOMI flux estimates over the campaign.

Comparison of total flux to sources detected aerially suggests that approximately 50% of emissions were contributed by super-emitters, consistent with previous analyses[13-15]. The number of unique super-emitting sources is small relative to the total infrastructure surveyed: 464 unique emission sources were detected at well sites, compressor stations, or gas plants, representing approximately 0.7% of infrastructure according to the Rextag database, and 65 unique pipeline sources (gathering and transmission) were detected, representing one detection per 420 kilometers of pipeline. This highlights the disproportionate contribution of super-emitters to regional emissions in the Permian Basin.

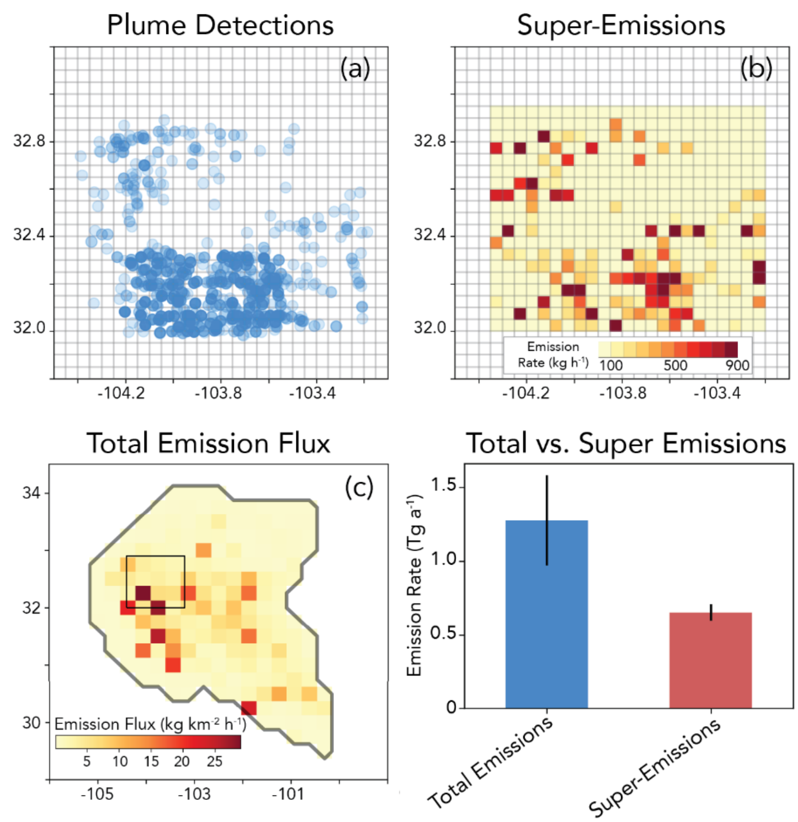

Figure 2. Methane results from the survey. (Panel a) Locations of unique aerial plume detections. (Panel b) Plume detections averaged to $0.05 \times 0.05°$ grid cells, following the methods described in the text. (Panel c) Total emission fluxes ($\sim 25 \times 25$ km^2) from the Permian Basin, derived from inversion of TROPOMI satellite observations. The inset black box represents the area surveyed during the airborne campaign. (Panel d) Comparison between emissions estimated by TROPOMI (inset black box in panel c) and super-emissions within the same area (panel b).

The multiple revisits of the Intensive Box show substantial variability in the "heavy-tail" of emission distributions across comprehensive scans. Figure 3a shows cumulative emission distributions for each complete and unique scan of the Intensive Box. Emissions quantified at instantaneous rates above 1000 kg h^{-1} account for 10-20% of total super-emissions for the first and second scans, while detections over this threshold account for 30-40% of total super-emissions for the third and fourth scans. Figure 3b shows the total emissions for each observation scan within the Intensive Box. Similarly, the total emissions estimated from the first and second scans (0.21-0.22 Tg a^{-1}) are 30-40% lower than those estimated from the third and fourth scans (0.32-0.35 Tg a^{-1}).

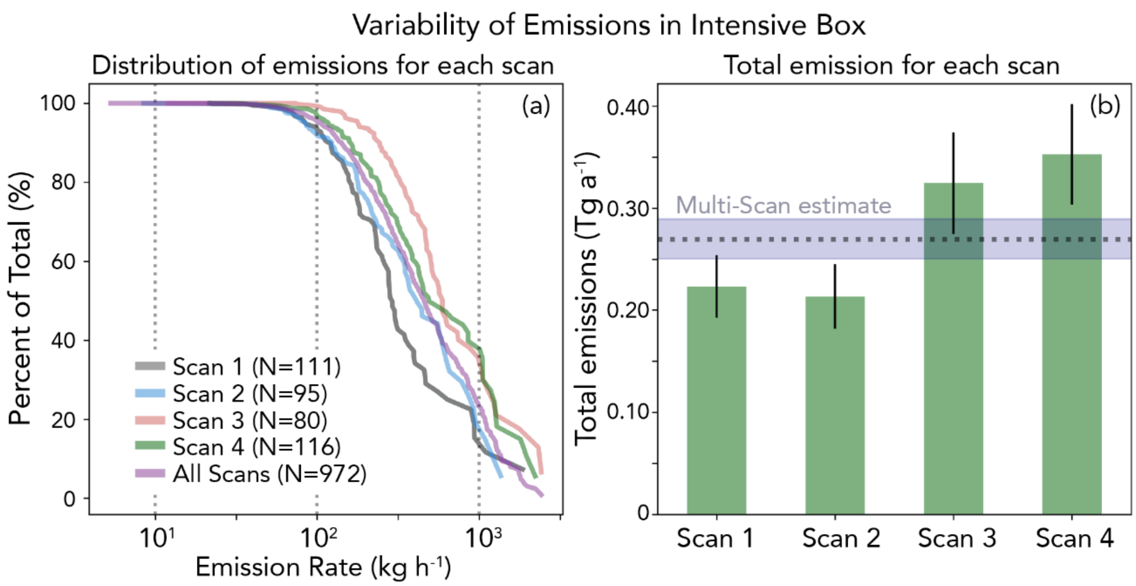

Figure 3. Variability assessment of Intensive Box. (Panel a) Cumulative distributions of emissions in the Intensive Box for each observational scan. (Panel b) Total emissions in the Intensive Box for each observational scan. The horizontal bar represents the estimated total emissions for the Intensive Box following the multi-scan aggregation procedure described in the text and shown in Figure 2.

There are multiple possible explanations for this observed variability. One possibility is inherent temporal variability in the underlying probability of super-emissions within a dense and complex basin like the Permian. While we cannot rule this out, another possibility is that although each scan includes measurements of all assets in the Intensive Box, the sample size remains relatively small, and the observed variability is simply due to expected statistical variability. Each scan of the Intensive Box resulted in 80-116 unique super-emitter detections, but only 2-11 detections above 1000 kg h^{-1}. Given that these emissions above 1000 kg h^{-1} can constitute up to 40% of the super-emitter total, it is entirely possible that the observed variability is largely explained by small sample size effects. When including all scans, the resulting distribution becomes smoother and more robust, with 972 total detections and 49 detections greater that 1000 kg h^{-1} contributing 23% to total super-emissions. This suggests that for basins with emissions size distributions similar to the Permian, reliably quantifying the upper tail of the distribution (>1000 kg h^{-1}), even within a relatively large sub-region, requires measuring all assets multiple times. For the middle section of the emissions size distribution, comprising emissions from approximately 100-1000 kg h^{-1}, observed results are more stable. Across the first four scans, estimated total emissions below 1000 kg h^{-1} range from 0.18-0.22 Tg a^{-1}, showing less variability than when considering the full emission distribution. This suggests that for emissions in this size range, a single comprehensive scan may be sufficient, at least for a region with an emissions size distribution similar to that of the Permian.

Comparing time-integrated event emissions to time-averaged totals

We detected 1380 individual plumes from 529 sources during the campaign. The Intensive Box contains 274 sources, from which we estimate 369 super-emitter events (Methods). A total of 174 super-emitter events both started and ended during the campaign (“finite” events); 18 emitted for the entirety of the campaign (“unbounded” events); and 177 either started during the campaign but were still emitting at the campaign’s end or were already emitting at the campaign start but ended before the campaign’s conclusion (“mixed” events). We associate durations for each super-emitter event, bounded by the shortest and longest possible event times estimated by direct observation (Methods). We then integrate the total emission for each event using the average emission rate estimated across all detections for that event and the estimated event duration.

Figure 4 shows the sum of emissions integrated from all detected events in the Intensive Box across the full campaign, using both shortest and longest possible event durations, and compares to the basin-level emission estimate (0.27 ± 0.02 Tg a^{-1}), integrated across the entirety of the campaign (12.7 ± 0.92 Gg), hereafter referred to as "Integrated Average." Integration of super-emitter events using the shortest duration results in 5.98 Gg, with 2.18 Gg (36%) from unbounded events, 2.44 Gg (41%) from mixed events, and 1.36 Gg (23%) from finite events. Integration using the longest durations results in higher total emissions (14.7 Gg), with 2.33 Gg (16%) from unbounded events, 5.21 Gg (35%) from mixed events, and 7.20 Gg (49%) from finite events.

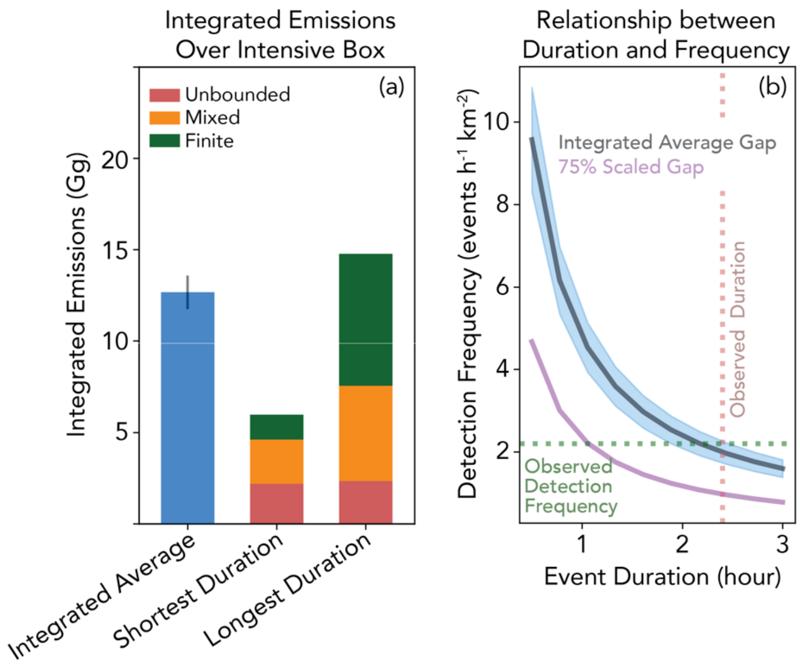

Figure 4. Results from estimating durations of super-emitter events in the Intensive Box. (Panel a) Total emissions from the Intensive Box (West and East Boxes combined, see Figure 1), integrated over the course of aerial survey, assuming either constant emissions ("Integrated Average", left bar), or integration from detected sources using the shortest or longest emission durations constrained directly by aerial observations (middle and right bars, respectively). (Panel b) Relationship between detection frequency and event duration during hours of non-observation needed to reconcile the emission gap estimate, derived by differencing the Integrated Average and Shortest Duration estimate (panel (a)) and described by Equation 1.

The Integrated Average is assumed to represent an unbiased estimate of total methane released during the survey, i.e., it statistically accounts for sources missed by the aircraft during hours of non-observation[2]. The time-integrated estimates under the shortest and longest duration assumptions represent the total emission contributions of events directly observed by the aircraft.

Therefore, the difference between the Integrated Average and time-integrated estimates represents the quantity of emissions anticipated but not directly observed. The difference between the Integrated Average estimate in Figure 3a and the shortest-duration time-integrated estimate reveals a 6.67 Gg gap in total emission estimates. In contrast, the difference between the Integrated Average and the longest-duration time-integrated results in an unrealistic -2.0 Gg surplus in emissions, indicating that the longest estimated event durations derived from observations is likely too large. These differences in gap estimates are driven by single-detection finite events that do not have a follow-up observation for an extended period, often days. Specifically, the median event duration for finite events using the shortest possible duration is 8.3 minutes, while the median under the longest duration assumption is 8500 minutes (141 hours).

To further test whether the estimated single-detection durations are representative, we performed an analysis for sources with multiple observations per day, where the spacing between the first plume detection and last observation (regardless of subsequent detection) was at least two hours (i.e., April 30, May 1, May 14-15; 230 sources total). Figure S2 shows the distribution of time differences between first and last detection for these sources. Sixty-nine percent of plume detections were followed by repeat detections at least two hours later, with a median duration of 2.4 hours. The 2.4-hour median is primarily set by observation revisit time, as only 2% of sources were observed more than three hours after the initial detection. Restricting this analysis to sources previously classified as finite (77 sources total) yields similar results, with median duration of 2.3 hours. This is suggestive that the 8.3 minute assumed duration for single-detection finite events is likely too low, and a characteristic super-emitter duration could be assumed to be at least 2.4 hours.

To further test the likelihood of longer (2+ hour) characteristic timescales for short-duration finite events, we create an empirical relationship to reconcile the emission gap with emission characteristics assumed during the time of non-observation. Specifically, the emission gap (G; units kg) can be reconciled through a set of non-observed events emitting at a characteristic emission rate Q (units kg h^{-1}), and characteristic duration D (units hours), during non-observed hours T (units hours), over an area A (km^2), related to the spatiotemporal frequency of events F (units events km^{-2} h^{-1}) via the following relationship:

$$F = \frac{G}{D * Q * T * A} \quad (1)$$

Figure 4b shows the outcome of F from Equation 1 assuming $Q = 150$ kg h^{-1} (e.g., the mode of the emission distribution in Figure S1.1), and $G = 6.67$ Gg, using a variety of event duration values D. Independent of Equation 1, Figure S1 suggests a characteristic median super-emitter emission duration of approximately 2.4 hours for observed finite events. Additionally, through analysis of plume detection timestamps and full-image acquisition geometries, we find that we detected 2.2 short-duration finite super-emitter events per hour per 100 km^2.

Coincidentally, in Figure 4b, the modeled non-observed event duration and detection frequencies from Equation 1 intersect the observed duration (2.4 hours) and detection frequency (2.2 events h^{-1} km^{-2}) values. This intersection supports the assumption that the population statistics observed during the survey likely continued similarly during non-observation hours. Therefore, Equation 1 provides a method to reconcile the gap between the Integrated Average and time-integrated emission estimates by recognizing the close relationship between duration and frequency, and how assumptions on one variable impact the other. For example, if one instead assumes that the gap in Figure 4a is driven entirely by short-duration super-emitter events missed by the aircraft, but further assumes that these event had very short average durations (~30 minutes), this implies a much higher frequency of super-emitters events during periods of non-observation (i.e., 9.6 events per hour per 100 km^2) than was actually observed during the survey, which may be unlikely.

Diurnal variability may also drive the size of the emission gap. A previous study using a network of continuously observing towers in the Permian showed that daytime-centric measurement studies may overestimate emissions in the Permian by as much as 27%, due to unaccounted diurnal variability[23]. To account for this, we can scale G in Equation 1 by 0.73 to represent possible diurnal effects. However, as shown in Figure 4b (purple curve), this adjustment eliminates the intersection point between candidate duration/frequency pairs and independent duration/frequency estimates, suggesting some combination of shorter event durations or fewer detections during unobserved hours. Ultimately further study with more continuous observations can help reduce lingering uncertainty. Since detection frequency and event duration are closely linked, future studies must balance observing systems that maximize spatial coverage with those that t maximizes temporal coverage.

Super-emitter duration by infrastructure type

Each source was attributed to broad infrastructure categories using simultaneously acquired 5 m visible imagery, asynchronously collected high resolution visible imagery (<1m) from Mapbox (www.mapbox.com), and the Rextag GIS database (Section S2). Sources were assigned to the following infrastructure categories: compressors, flares, tanks, and pipelines (gathering or transmission). We also classified sources that do not fall into those categories but that were clearly located within the footprint of a well site or gas plant as “other well site” and “other gas plant,” respectively. Lastly, any sources for which a clear infrastructure designation could not be made, due to a combination of incomplete GIS information or unclear visible imagery, were classified as “other.” Figure 5a shows the breakdown of sources attributed to infrastructure categories across both the entire survey domain and the Intensive Box. Compressors constitute the majority of detected sources across the full survey domain (27%) and represent a significant fraction of sources (25-39%) across duration categories in the Intensive Box. Combined with pipelines, these sources together make up 39% of all sources detected. These results highlight sustained, large emission activity associated with gathering and boosting activities in the Permian, a pattern that has been noted in multiple measurement surveys dating back to 2019[14,25,26]. After compressors, the most prevalent source categories are other well-sites (24%), tanks (22%), pipelines (12%), flares (11%), and other gas plant sources (2%).

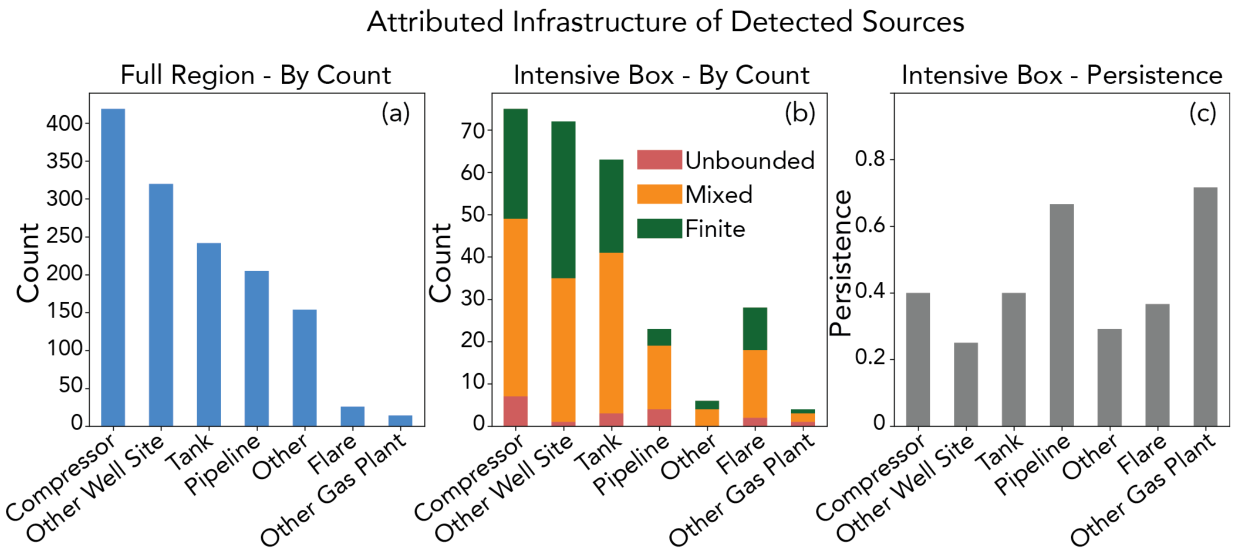

Figure 5. Infrastructure counts for detected sources during the campaign. (Panel a) Infrastructure counts for sources across the entire survey spatial domain. (Panel b) Infrastructure counts for sources in the Intensive Box, broken out by super-emitter duration category. (Panel c) Median persistence (number of detections divided by number of observations) for infrastructure in the Intensive Box.

Across super-emitter event duration classes within the Intensive Box, there is some slight variation in infrastructure prevalence (Figure 5b). For example, among finite events, other well-site emissions are more prevalent (36% of all finite sources) than compressors (25%), whereas across unbounded events, well-site events are much less prevalent (6% of unbounded sources) compared to compressors (39%). Using a related metric, source persistence or detection frequency (number of detections divided by number of overpasses) (Figure 5c), other well-site sources are more intermittent (median 25%) than any other source category. This, along with their high prevalence among finite-duration events, suggests that these detections are generally shorter-lived and potentially associated with planned or known operations. In contrast, attributed tank sources, many of which are located at well-sites, are more persistent (40%) and have lower prevalence among finite events than other well-site emissions: 22% of tank sources pertain to the finite class, compared to 36% of other well-site emissions. Emissions from tanks can results from a variety of causes, ranging from short-lived safety events (e.g., flashings) to longer-lived operation inefficiencies (e.g., open hatches, leaks). The observations of more persistent, longer-lived tank emission suggests that a subset of these sources pertain to the latter category, meaning that focused attention on these sources could potentially lead to significant emission reduction.

Discussion

Facility-scale point source super-emitter observations support multiple use cases: (1) improving estimation of total emissions at the basin scale, (2) enhancing internal or external operator reporting of emissions, and (3) identifying and prioritizing emission mitigation opportunities. For the first use case (basin-scale emission estimation), understanding the contribution of super-emissions to the basin total requires several key observational constraints, including detection sensitivity to a critical range of super-emitters (i.e., DL ~100 kg h^{-1}) and broad spatial sampling across a basin to capture the inherent low frequency of these emitters. In absence of these two observing requirements, layers of inference can be used to fill in spatial and sensitivity gaps, but such inference may introduce bias and misrepresent the impact of large emission sources on regional emissions. This study observed all infrastructure and production on the New Mexico side of the Permian Basin during an 18-day campaign, capturing representative statistics on super-emitters during the observation period. We estimate that super-emitters account for 50% of total emissions in this domain, highlighting the disproportionate impact, consistent with previous studies using independent measurement systems[2,15,27].

Reporting programs like GHGRP Subpart W rely on event duration for the reporting of large emission events. Operator information from known process events or data from supervisory control and data acquisition (SCADA) systems can be valuable for estimating event durations. However, in many cases, operators may not have detailed information from all emission events[28], especially in instances of unexpected leaks or malfunctions. In these cases, atmospheric observations can be useful for filling gaps by independently quantifying event durations. Nevertheless, a fundamental limitation of current observing systems is the inability to simultaneously provide the spatial coverage needed to estimate basin-level super-emitter contributions and the temporal resolution required to constrain the duration of individually events. In this study we estimated event durations directly from aerial observations, focusing on areas of the Permian that were observed repeatedly (the Intensive Box). Integration of these events using the shortest and longest possible event durations results in total emissions ranging from 5.98 to 14.7 Gg CH_4. When isolating to the unbounded category, where we have the greatest confidence in emission duration, we find that mitigation of these 18 sources, most of which are from compressors, would result in sizable emission and cost reductions (6,180 ± 2,100 kg h^{-1}).

Overall, we demonstrated that frequent wide-area monitoring of oil & gas basins for super-emitters uncovers a diverse array of processes, infrastructure types, emission magnitudes, and event durations. We find evidence suggesting that characteristic super-emitter durations are often on the scale of hours. Ultimately, leveraging a tiered observing system that uses multiple technologies and vetted data sources (e.g., operator reports) can further reduce quantification uncertainty across the oil & gas supply chain. Frequent aerial surveys provide both the spatial breadth and revisit frequency needed to build evidence of characteristic duration and emission magnitude, which are key for validating reporting programs and identifying areas for immediate mitigation.

Methods

Super-emitter event duration calculation

Super-emitter event durations are estimated directly from repeat aerial observations, with a focus on the East and West Boxes, where multiple overpasses were made over the course of the campaign. To classify site-level sources, we cluster plume detections in space, time, and by infrastructure using a DBSCAN algorithm with a local neighborhood of 250-m[29]. We then classify super-emitter events by the binary detection outcome of each observation for each source. If a detection follows a non-detection, it constitutes the start of a new event. If a non-detection follows a detection, it constitutes the end of an event. A single emission source can therefore have multiple super-emitter events. For events whose first or last observation results in a detection (or both), the duration of the event is unbounded, meaning we have no information to suggest how much longer earlier or later relative to the campaign, the emission event started or ended, respectively.

This process of super-emitter event identification from direct observation results in four categories: (1) *finite*, meaning we observed the beginning and end of the event; (2) *unbounded start*, meaning the first observation resulted in a detection, but the event ended before the campaign concluded; (3) *unbounded end*, meaning the event was observed to start during the campaign, but the last observation was a detection; and (4) *unbounded*, meaning that all observations resulted in a detection. For the sake of comparison in this manuscript, we group unbounded end and unbounded start events together to make a *mixed* category.

Durations for each event are constrained to the shortest and longest possible lengths based on observations. For example, if a source was observed four times, and only the second and third observations resulted in detections, this would constitute a finite event, with the shortest possible duration being the time elapsed between second and third observations and the longest possible duration being the time between the first and fourth observations. In this example, it is possible that the source temporarily stopped emitting between the second and third observations, which was not observed. Had it been observed, it would have resulted in two distinct events with total durations shorter than this single event duration. However, this potential bias is assumed to be negated by cases of non-detections between successive observations when, in reality, there may have been a temporary super-emitter event went undetected. Therefore, for the purpose of this study, we follow the duration estimation procedure as described above and assume that missed detections and non-detections between site observations are equally likely. Further study with distributed CEMS systems or more intensive aerial survey could reduce lingering uncertainty related to these assumptions, presuming they are representative of all infrastructure in a basin.

For unbounded cases, we restrict the duration to either the campaign start or end for the purpose of understanding emissions strictly within the time domain of the aerial campaign itself. For example, for an unbounded start event where the first observation resulted in a detection and the second observation a non-detection, the shortest possible duration would be near-instantaneous given the single snapshot detection, and the longest possible duration would be the time elapsed between the start of the campaign (first observation of any site) and the second observation. Technically, a shortest duration could be estimated from a two-dimension plume image itself, as the concentration at the tail of an observed plume must have traveled from the source's origin over a period of time. However, rigorous estimation of these lengths scales would require complex atmospheric modeling, and in cases of remote sensing, the true spatial atmospheric distribution of a plume is anticipated to be longer than what is observed by a sensor, as an observing system will have difficulty distinguishing concentration enhancements below its instrument's sensitivity. For examples where the super-emitter event only contained a single detection, we assume an 8.3-minute shortest duration, as that represents the minimum nonzero event duration based on observations from this survey and is within the range of durations described by a previous study[18].

TROPOMI flux inversion

We use the Integrated Methane Inversion (IMI) version 2.0[22] to quantify total Permian methane emissions during the study period, using TROPOMI observations from the blended TROPOMI+GOSAT retrieval product[30]. Emissions are inferred at 0.25° × 0.25° resolution for 200 grid elements across the basin (Figure 2c) and at coarser resolution for 16 buffer elements outside the basin, which serve to capture external emissions and pad the rectangular inversion domain (26.5°N–37°N, 97.1875°W–108.125°W). The inversion also optimizes the boundary conditions along the four cardinal edges of the domain. We use the IMI 2.0 default prior emission estimates and assume lognormal error statistics on emissions[31]. We use the default IMI 2.0 values for prior errors (a uniform geometric standard deviation of 2 for all emission elements), observational errors (15 ppb), and regularization parameter (γ=1).

Competing Interests

The authors declare no conflicts of interest.

Acknowledgements

The Carbon Mapper team acknowledges the support of their sponsors including the High Tide Foundation, Bloomberg Philanthropies, and other philanthropic donors. The Global Airborne Observatory (GAO) is managed by the Center for Global Discovery and Conservation Science at

Arizona State University. The GAO is made possible by support from private foundations, visionary individuals, and Arizona State University. Portions of this work were funded by the NASA Carbon Monitoring System. This work was partially supported by the California Energy Commission (SUMMATION project, agreement number PIR-17-015). It does not necessarily represent the views of the Energy Commission, its employees, or the State of California. The Energy Commission, the State of California, its employees, contractors, and subcontractors make no warranty, express or implied, and assume no legal liability for the information in this report; nor does any party represent that the uses of this information will not infringe upon privately owned rights. This paper has not been approved or disapproved by the California Energy Commission, nor has the California Energy Commission passed upon the accuracy or adequacy of the information in this paper. This manuscript has been authored by authors at Lawrence Berkeley National Laboratory under Contract No. DE-AC02-05CH11231 with the U.S. Department of Energy. The U.S. Government retains, and the publisher, by accepting the article for publication, acknowledges, that the U.S. Government retains a non-exclusive, paid-up, irrevocable, world-wide license to publish or reproduce the published form of this manuscript, or allow others to do so, for U.S. Government purposes.

Data Availability

Plume datasets are available via Carbon Mapper's Public Data Portal (data.carbonmapper.org). The IMI source code is available online (https://carboninversion.com/). Analysis code for this manuscript will be posted publicly upon acceptance of the manuscript.

Author Contributions

D.H.C designed the study, performed the main analysis, and wrote the manuscript. D.B, A.A, R.M.D performed additional analyses of plume datasets. G.P.A and J.H. acquired GAO data. D.J.V performed the TROPOMI regional flux inversion. E.D.S. and S.C.B. performed additional statistical and uncertainty analyses. All authors provided feedback on the manuscript.

References

1. EPA, Standards of Performance for New, Reconstructed, and Modified Sources and Emissions Guidelines for Existing Sources: Oil and Natural Gas Sector Climate Review, 40 CFR Part 60, URL https://www.federalregister.gov/documents/2024/03/08/2024-00366/standards-of-performance-for-new-reconstructed-and-modified-sources-and-emissions-guidelines-for. Last accessed: Mar 10, 2025

2. Sherwin, E.D., Rutherford, J.S., Zhang, Z., Chen, Y., Wetherley, E.B., Yakovlev, P.V., Berman, E.S., Jones, B.B., Cusworth, D.H., Thorpe, A.K. and Ayasse, A.K., 2024. US oil and gas system emissions from nearly one million aerial site measurements. *Nature*, *627*(8003), pp.328-334.

3. Naus, S., Maasakkers, J.D., Gautam, R., Omara, M., Stikker, R., Veenstra, A.K., Nathan, B., Irakulis-Loitxate, I., Guanter, L., Pandey, S. and Girard, M., 2023. Assessing the relative importance of satellite-detected methane superemitters in quantifying total emissions for oil and gas production areas in algeria. *Environmental Science & Technology*, *57*(48), pp.19545-19556.

4. Lauvaux, T., Giron, C., Mazzolini, M., d'Aspremont, A., Duren, R., Cusworth, D., Shindell, D. and Ciais, P., 2022. Global assessment of oil and gas methane ultra-emitters. *Science*, *375*(6580), pp.557-561.

5. Cusworth, D.H., Thorpe, A.K., Ayasse, A.K., Stepp, D., Heckler, J., Asner, G.P., Miller, C.E., Yadav, V., Chapman, J.W., Eastwood, M.L. and Green, R.O., 2022. Strong methane point sources contribute a disproportionate fraction of total emissions across multiple basins in the United States. *Proceedings of the National Academy of Sciences*, *119*(38), p.e2202338119.

6. Pandey, S., Worden, J., Cusworth, D.H., Varon, D.J., Thill, M.D., Jacob, D.J. and Bowman, K.W., 2024. Relating Multi-Scale Plume Detection and Area Estimates of Methane Emissions: A Theoretical and Empirical Analysis. https://doi.org/10.31223/X52M54

7. Omara, M., Zavala-Araiza, D., Lyon, D.R., Hmiel, B., Roberts, K.A. and Hamburg, S.P., 2022. Methane emissions from US low production oil and natural gas well sites. *Nature Communications*, *13*(1), p.2085.

8. Williams, J.P., Omara, M., Himmelberger, A., Zavala-Araiza, D., MacKay, K., Benmergui, J., Sargent, M., Wofsy, S.C., Hamburg, S.P. and Gautam, R., 2024. Small emission sources disproportionately account for a large majority of total methane emissions from the US oil and gas sector. *EGUsphere*, *2024*, pp.1-31.

9. Chen, Z., El Abbadi, S.H., Sherwin, E.D., Burdeau, P.M., Rutherford, J.S., Chen, Y., Zhang, Z. and Brandt, A.R., 2024. Comparing Continuous Methane Monitoring Technologies for High-Volume Emissions: A Single-Blind Controlled Release Study. *ACS ES&T Air*.

10. Conrad, B.M., Tyner, D.R., Li, H.Z., Xie, D. and Johnson, M.R., 2023. A measurement-based upstream oil and gas methane inventory for Alberta, Canada reveals higher emissions and different sources than official estimates. *Communications Earth & Environment*, *4*(1), p.416.

11. Johnson, M.R., Conrad, B.M. and Tyner, D.R., 2023. Creating measurement-based oil and gas sector methane inventories using source-resolved aerial surveys. *Communications Earth & Environment*, *4*(1), p.139.

12. Kunkel, W.M., Carre-Burritt, A.E., Aivazian, G.S., Snow, N.C., Harris, J.T., Mueller, T.S., Roos, P.A. and Thorpe, M.J., 2023. Extension of methane emission rate distribution for Permian Basin oil and gas production infrastructure by aerial LiDAR. *Environmental Science & Technology*, *57*(33), pp.12234-12241.

13. Cusworth, D.H., Duren, R.M., Thorpe, A.K., Olson-Duvall, W., Heckler, J., Chapman, J.W., Eastwood, M.L., Helmlinger, M.C., Green, R.O., Asner, G.P. and Dennison, P.E., 2021. Intermittency of large methane emitters in the Permian Basin. *Environmental Science & Technology Letters*, *8*(7), pp.567-573.

14. Chen, Y., Sherwin, E.D., Berman, E.S., Jones, B.B., Gordon, M.P., Wetherley, E.B., Kort, E.A. and Brandt, A.R., 2022. Quantifying regional methane emissions in the New Mexico Permian Basin with a comprehensive aerial survey. *Environmental science & technology*, *56*(7), pp.4317-4323.

15. Sherwin, E., Kruguer, J., Wetherley, E.B., Yakovlev, P.V., Brandt, A., Deiker, S., Berman, E.S. and Biraud, S., Comprehensive Aerial Surveys Find a Reduction in Permian Basin Methane Intensity from 2020-2023. *Available at SSRN 5087216*.

16. El Abbadi, S.H., Chen, Z., Burdeau, P.M., Rutherford, J.S., Chen, Y., Zhang, Z., Sherwin, E.D. and Brandt, A.R., 2024. Technological Maturity of Aircraft-Based Methane Sensing for Greenhouse Gas Mitigation. *Environmental Science & Technology*.
17. EPA. Petroleum and Natural Gas Systems Subpart W, Greenhouse Gas Reporting Program URL https://www.epa.gov/system/files/documents/2025-01/w_petroleumnaturalgassystems_infosheet_2024.pdf, Last accessed Feb 6, 2025
18. Yang, S. and Ravikumar, A., 2024. Assessing the Performance of Continuous Methane Monitoring Systems at Midstream Compressor Stations. DOI 10.26434/chemrxiv-2024-qfdbh
19. Ayasse, A.K., Cusworth, D., O'Neill, K., Fisk, J., Thorpe, A.K. and Duren, R., 2023. Performance and sensitivity of column-wise and pixel-wise methane retrievals for imaging spectrometers. *Atmospheric Measurement Techniques*, *16*(24), pp.6065-6074.
20. Veefkind, J.P., Aben, I., McMullan, K., Förster, H., De Vries, J., Otter, G., Claas, J., Eskes, H.J., De Haan, J.F., Kleipool, Q. and Van Weele, M., 2012. TROPOMI on the ESA Sentinel-5 Precursor: A GMES mission for global observations of the atmospheric composition for climate, air quality and ozone layer applications. *Remote sensing of environment*, *120*, pp.70-83.
21. Varon, D.J., Jacob, D.J., Hmiel, B., Gautam, R., Lyon, D.R., Omara, M., Sulprizio, M., Shen, L., Pendergrass, D., Nesser, H. and Qu, Z., 2022. Continuous weekly monitoring of methane emissions from the Permian Basin by inversion of TROPOMI satellite observations. *Atmospheric Chemistry and Physics Discussions*, *2022*, pp.1-26.
22. Estrada, L.A., Varon, D.J., Sulprizio, M., Nesser, H., Chen, Z., Balasus, N., Hancock, S.E., He, M., East, J.D., Mooring, T.A. and Oort Alonso, A., 2024. Integrated Methane Inversion (IMI) 2.0: an improved research and stakeholder tool for monitoring total methane emissions with high resolution worldwide using TROPOMI satellite observations. *EGUsphere*, *2024*, pp.1-31.
23. Barkley, Z.R., Davis, K.J., Miles, N.L. and Richardson, S.J., 2024. Examining Daily Temporal Characteristics of Oil and Gas Methane Emissions in the Delaware Basin Using Continuous Tower Observations. *Authorea Preprints*.

24. Zaimes, G.G., Littlefield, J.A., Augustine, D.J., Cooney, G., Schwietzke, S., George, F.C., Lauderdale, T. and Skone, T.J., 2019. Characterizing regional methane emissions from natural gas liquid unloading. *Environmental science & technology*, *53*(8), pp.4619-4629.
25. Lyon, D.R., Hmiel, B., Gautam, R., Omara, M., Roberts, K.A., Barkley, Z.R., Davis, K.J., Miles, N.L., Monteiro, V.C., Richardson, S.J. and Conley, S., 2021. Concurrent variation in oil and gas methane emissions and oil price during the COVID-19 pandemic. *Atmospheric Chemistry and Physics*, *21*(9), pp.6605-6626.
26. Warren, J.D., Sargent, M., Williams, J.P., Omara, M., Miller, C.C., Roche, S., MacKay, K., Manninen, E., Chulakadabba, A., Himmelberger, A. and Benmergui, J., 2024. Sectoral contributions of high-emitting methane point sources from major US onshore oil and gas producing basins using airborne measurements from MethaneAIR. *EGUsphere*, *2024*, pp.1-22.
27. Guanter, L., Warren, J., Omara, M., Chulakadabba, A., Roger, J., Sargent, M., Franklin, J.E., Wofsy, S.C. and Gautam, R., 2025. Remote sensing of methane point sources with the MethaneAIR airborne spectrometer. *EGUsphere*, *2025*, pp.1-22.
28. Zimmerle, D., Dileep, S. and Quinn, C., 2024. Unaddressed Uncertainties When Scaling Regional Aircraft Emission Surveys to Basin Emission Estimates. *Environmental Science & Technology*, *58*(15), pp.6575-6585
29. Schubert, E., Sander, J., Ester, M., Kriegel, H.P. and Xu, X., 2017. DBSCAN revisited, revisited: why and how you should (still) use DBSCAN. *ACM Transactions on Database Systems (TODS)*, *42*(3), pp.1-21.
30. Balasus, N., Jacob, D.J., Lorente, A., Maasakkers, J.D., Parker, R.J., Boesch, H., Chen, Z., Kelp, M.M., Nesser, H. and Varon, D.J., 2023. A blended TROPOMI+ GOSAT satellite data product for atmospheric methane using machine learning to correct retrieval biases. *Atmospheric Measurement Techniques*, *16*(16), pp.3787-3807.
31. Hancock SE, Jacob D, Chen Z, Nesser H, Davitt A, Varon DJ, Sulprizio MP, Balasus N, Estrada LA, East JD, Penn E. Satellite quantification of methane emissions from South American countries: A high-resolution inversion of TROPOMI and GOSAT observations. EGUsphere. 2024 Jun 24;2024:1-33.

630

Supporting Information

Section S1. Probability of Detection (POD) during campaign

We assess the distribution of emissions during the campaign to provide an empirical estimate of the instrument+retrieval+detection algorithm's detection performance at the altitude flown during the survey (roughly 5 km). We do this by plotting the fraction of sources vs the emission rate distribution on a log10 scale and assessing where the distribution diverges from linearity (i.e. power law behavior). Numerous methane remote sensing studies find evidence of power law behavior among super-emitters (Sherwin et al., 2024; Lauvaux et al., 2022; Loitxate et al., 2022). These analyses apply the Monte Carlo approach introduced in Sherwin et al. (2024) and described further as a "source instantaneous" analysis in Appendix F.1 of Sherwin et al. (2025) The point of divergence can roughly be assumed to represent the area where the instrument+retrieval+detection algorithm begins to non-reliably detect all emission sources. Figure S1.1 shows this distribution for the entire survey domain, Figure S1.2 shows the distribution for the Intensive Box, and Figure S1.3 shows the distribution for the peripheral non-Intensive areas.

Wind speed can influence detection capabilities, with higher wind speeds rendering the same methane flux rates more difficult to detect (Conrad et al., 2023)~~.~~. The peripheral areas were flown under average 3.5 m/s wind speed, while the Intensive Box was flown under average 3.1 m/s wind speed. From inspection of Figures S1.1-S1.3, we see divergence from linearity occurring between 90-150 kg h^{-1}. Therefore, for the sake of this study, we assume that we either exceed or have near full detection capability to all super-emitting sources.

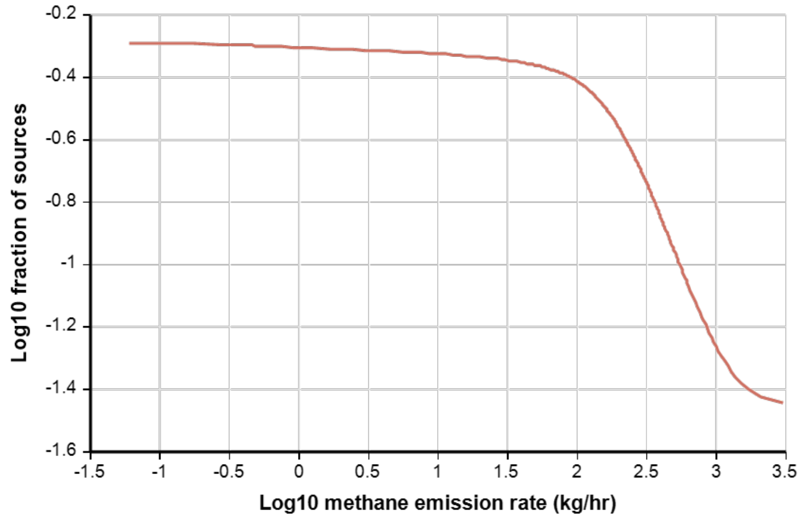

Figure S1.1. Distribution of plume detection in the full survey domain

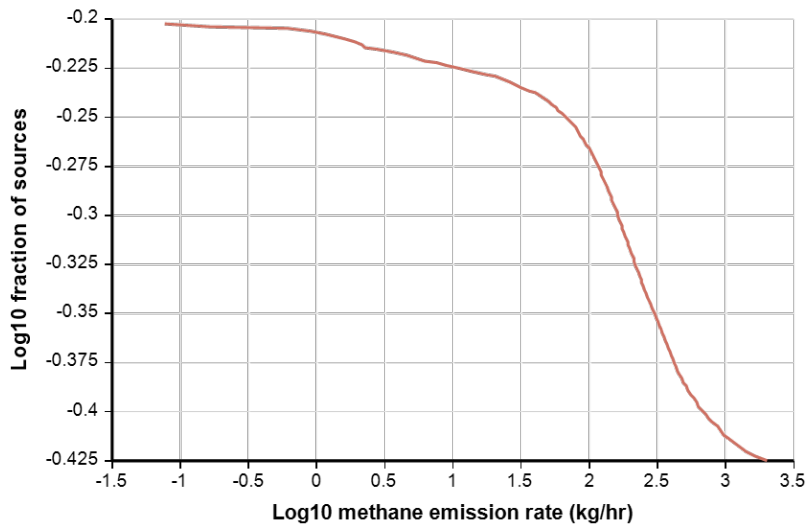

Figure S1.2. Distribution of plume detection in the Intensive Box

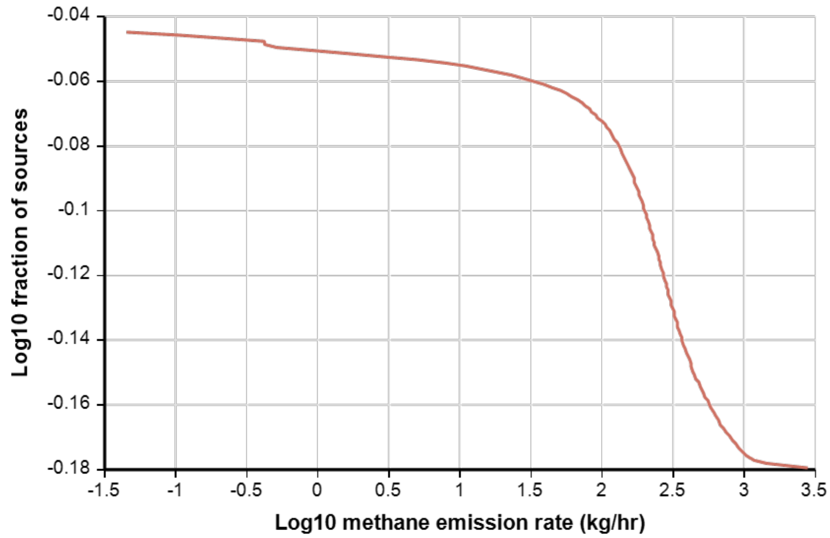

Figure S1.3. Distribution of plume detection peripheral areas (non-Intensive Box in NM).

References for this Section

Sherwin, E.D., Rutherford, J.S., Zhang, Z., Chen, Y., Wetherley, E.B., Yakovlev, P.V., Berman, E.S., Jones, B.B., Cusworth, D.H., Thorpe, A.K. and Ayasse, A.K., 2024. US oil and gas system emissions from nearly one million aerial site measurements. Nature, 627(8003), pp.328-334.

Lauvaux, T., Giron, C., Mazzolini, M., d'Aspremont, A., Duren, R., Cusworth, D., Shindell, D. and Ciais, P., 2022. Global assessment of oil and gas methane ultra-emitters. Science, 375(6580), pp.557-561.

Irakulis-Loitxate, I., Guanter, L., Maasakkers, J.D., Zavala-Araiza, D. and Aben, I., 2022. Satellites detect abatable super-emissions in one of the world's largest methane hotspot regions. Environmental science & technology, 56(4), pp.2143-2152.

Sherwin, E., Kruguer, J., Wetherley, E.B., Yakovlev, P.V., Brandt, A., Deiker, S., Berman, E.S. and Biraud, S., Comprehensive Aerial Surveys Find a Reduction in Permian Basin Methane Intensity from 2020-2023. Available at SSRN 5087216.

Conrad, B.M., Tyner, D.R. and Johnson, M.R., 2023. Robust probabilities of detection and quantification uncertainty for aerial methane detection: Examples for three airborne technologies. *Remote Sensing of Environment*, *288*, p.113499.

Section S2. Basin quantification sensitivity tests.

Section S2.1 Sensitivity to grid resolution

Figures 1 and 2 from the main manuscript show the super-emitter basin-level estimate, derived from discretizing the basin into 0.05° × 0.05° grid cell boxes over which plumes were summed and averaged. Figure S1.1 shows the sensitivity of that basin estimate when we vary the grid size between 0.03° to 0.10°. Some variation is present, which is driven by the intersection of individual flight geometries against specified grid geometries. For example, too large of a grid cell may result in an incomplete full scan over that AOI in a given day. That partial scan would not be included in the average estimate. However, in Figure S1.1 each estimate is consistent within uncertainties of all other estimates.

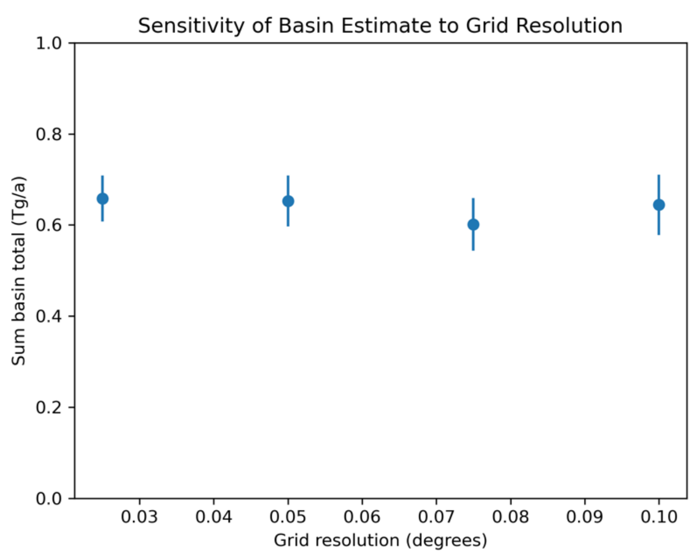

Figure S1.1. Sensitivity of super-emitter basin estimate to grid resolution.

Section S2.2 Sensitivity to quantification algorithm

We test the basin-level quantification methods described in the main manuscript with alternative quantitative approaches. Specifically, following reference 2 in the main manuscript (Sherwin et al., 2024), we apply a Monte Carlo approach to quantify emissions by sampling from the observed emission distribution for each source. Table S2.1 Shows the result of this alternative approach compared to the methods described in this study. Both methods produce strikingly similar estimates across the full survey domain and within sub-basin regions of the full domain.

Table S2.1 Comparison of emission estimates derived for regions of the campaign

Region	Emission Estimate (Tg a^{-1}) (This Study)[1]	Emission Estimate (Tg a^{-1}) (application of Sherwin et al., 2024)[2]
Full Domain	0.65 ± 0.06	0.65 (0.62-0.68)
West Box	0.14 ± 0.01	0.13 (0.12-0.14)
East Box	0.17 ± 0.03	0.17 (0.15-0.18)
Intensive Box (East + West Boxes)	0.27 ± 0.02	0.30 (0.28-0.32)
Peripheral Box	0.35 ± 0.04	0.34 (0.31-0.36)

[1]Uncertainties reported as 1-sigma
[2]Uncertainties reported as 95% confidence intervals

Section S3. Attribution to infrastructure

All plume datasets are available as an attachment to this manuscript and are available on Carbon Mapper's Data Portal (data.carbonmapper.org). Each plume was individually attributed to infrastructure using a combination of visible imagery acquired from GAO imaging spectrometer, high resolution basemap imagery from Mapbox (https://www.mapbox.com), and the Rextag oil & gas infrastructure database (https://www.rextag.com). Below are example plumes taken from Carbon Mapper's Data Portal, attributed to the infrastructure categories described in the text, underlaid with Mapbox imagery.

S2.1 Compressors

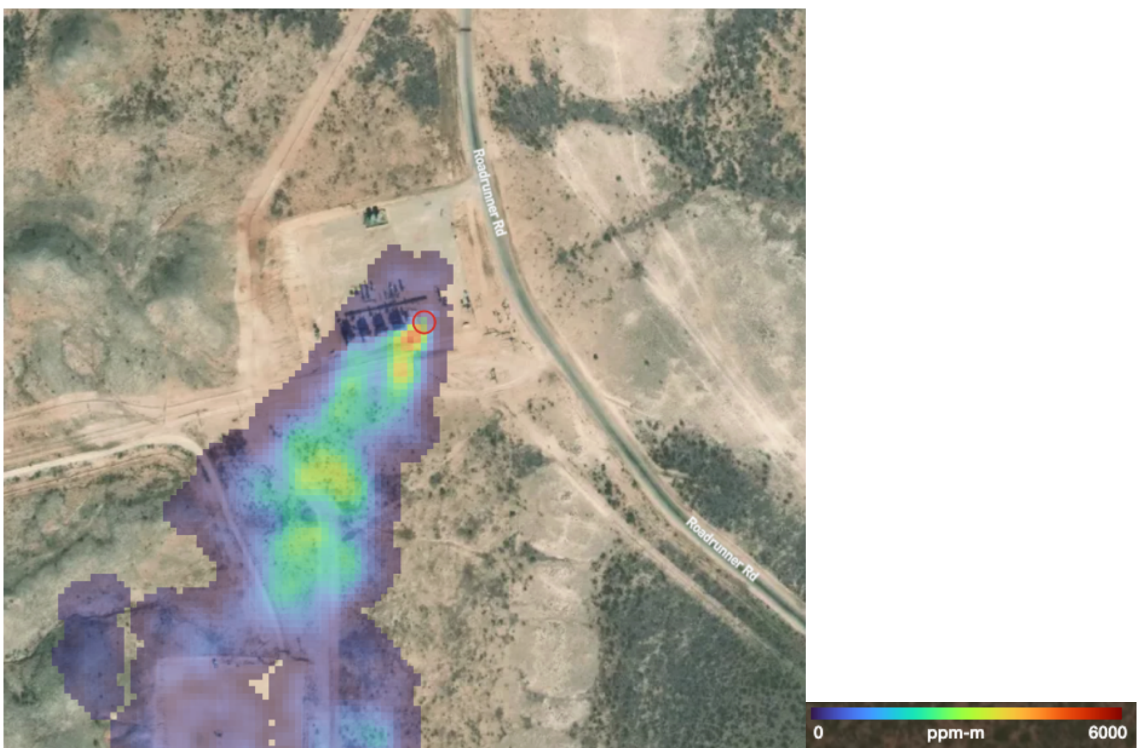

Figure S2.1.1 GAO20240513t172418p0000-A

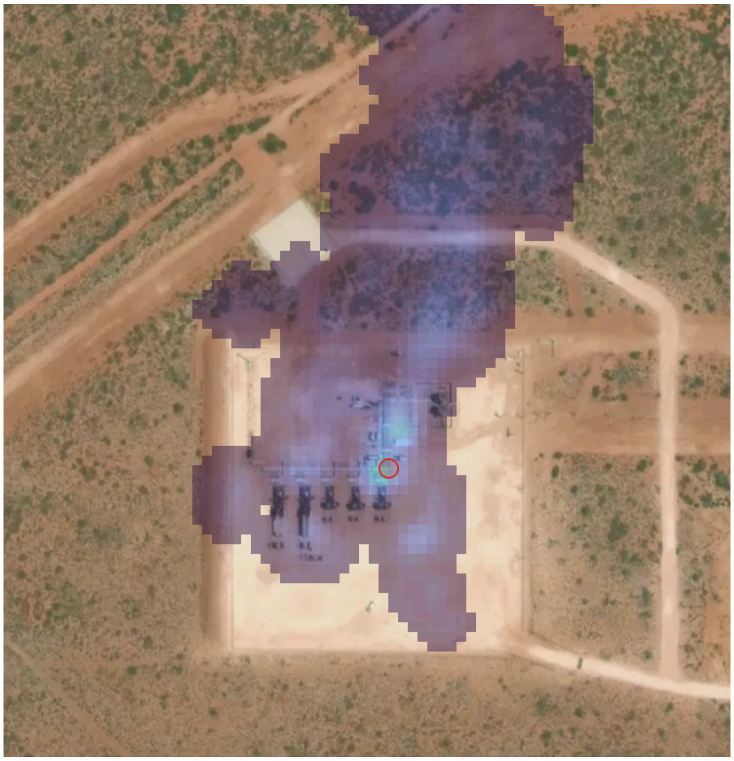

Figure S2.1.2. GAO20240514t183045p0000-G

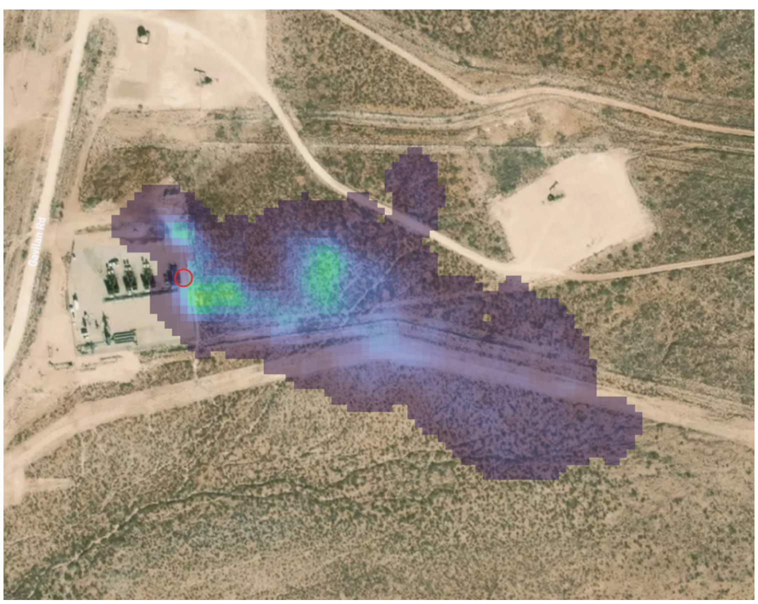

Figure S2.1.3. GAO20240517t172646p0000-A

S2.2. Flares

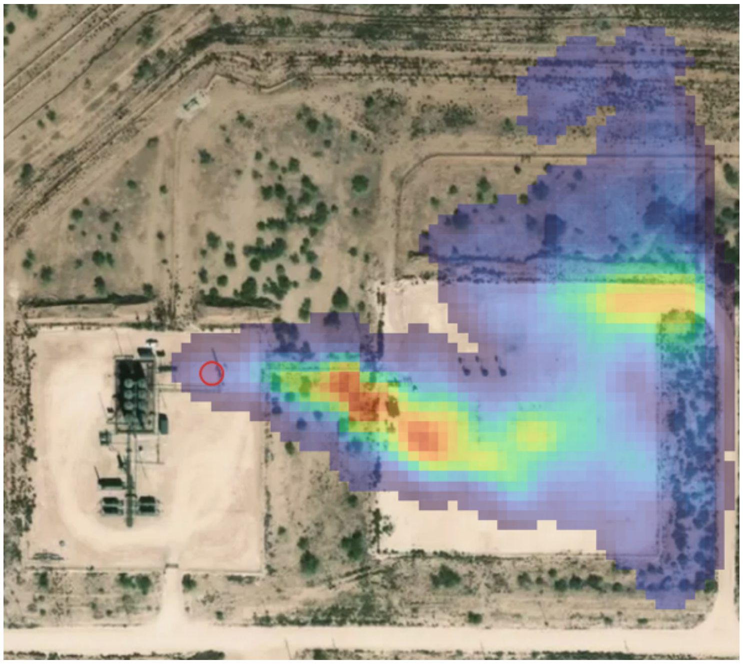

Figure S2.2.1 GAO20240517t163411p0000-G

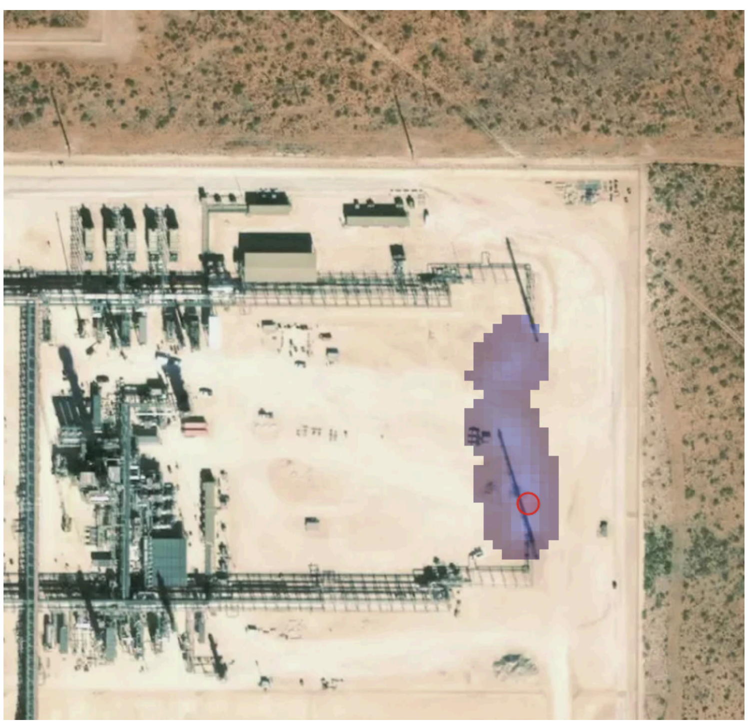

Figure S2.2.2 GAO20240430t174249p0000-I

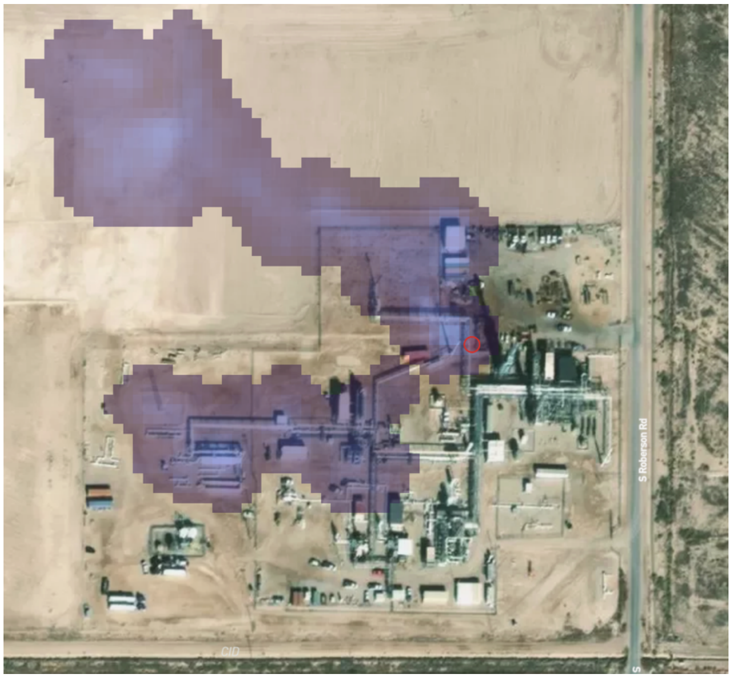

Figure S2.2.3 GAO20240501t183708p0000-B

S2.3. Pipelines

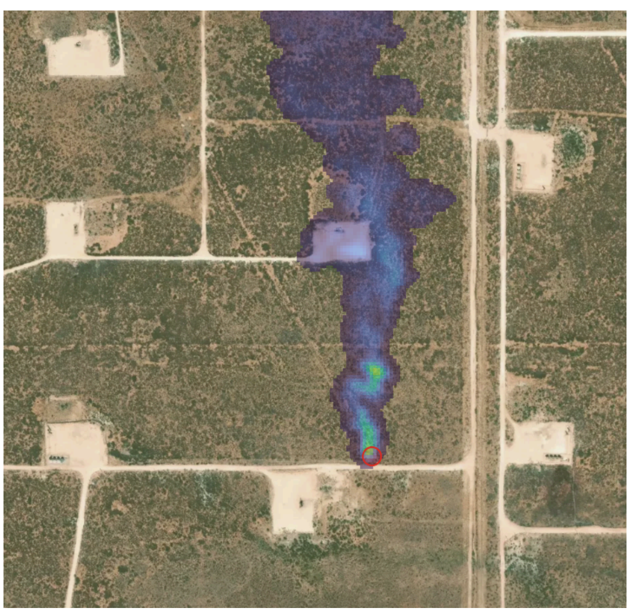

Figure S2.3.1 GAO20240430t162033p0000-Q

Figure S2.3.2 GAO20240507t171126p0001-B

Figure S2.3.3 GAO20240515t181635p0000-E

S2.4. Tanks

Figure S2.4.1 GAO20240513t155454p0000-F

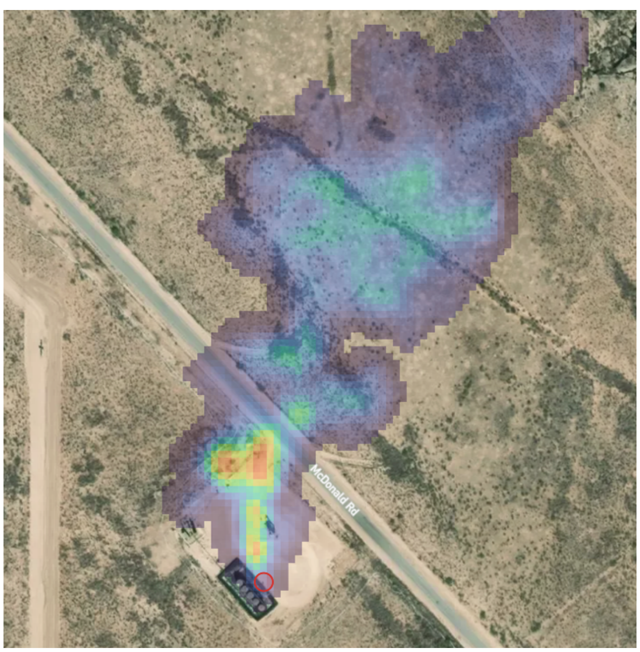

Figure S2.4.2 GAO20240515t180844p0000-B

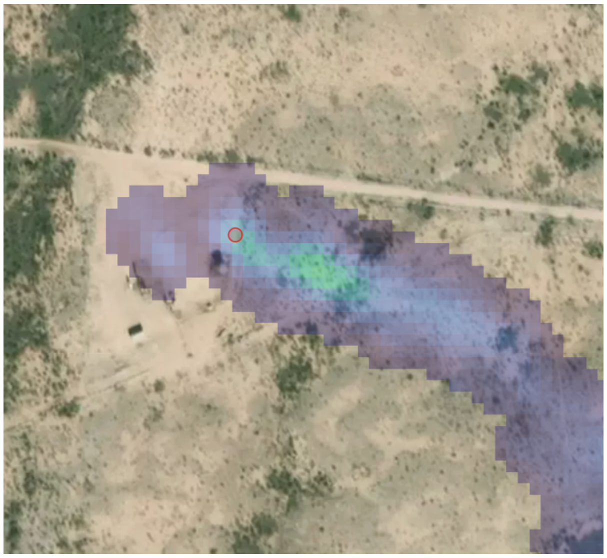

Figure S2.4.3 GAO20240509t153040p0000-B

S2.5. Other Well-Site

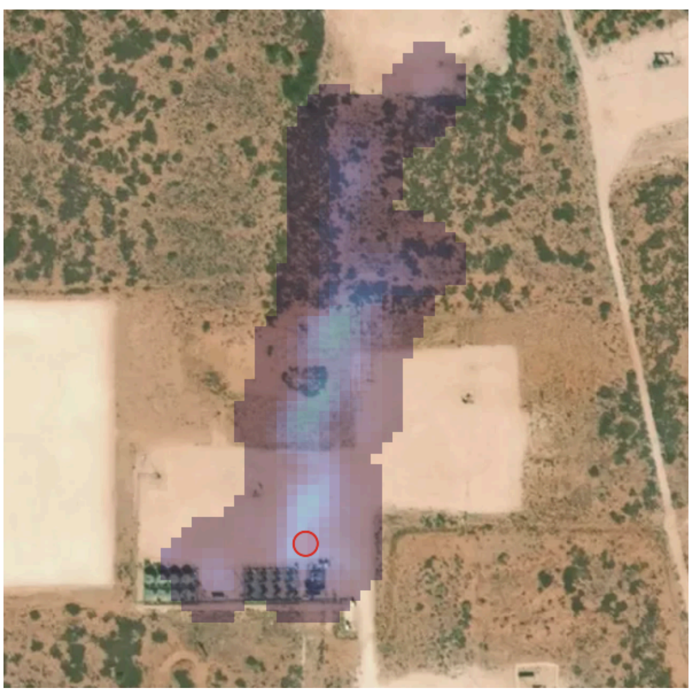

Figure S2.5.1 GAO20240430t191638p0000-A

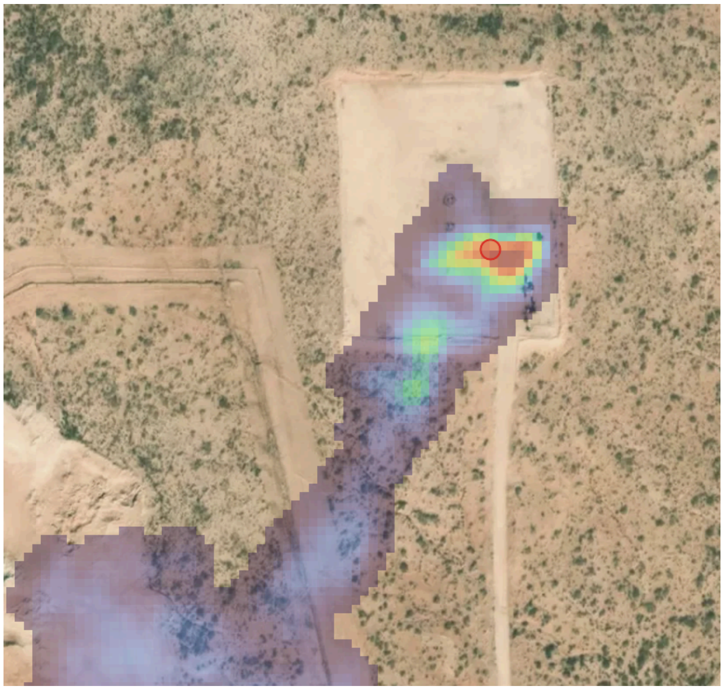

Figure S2.5.2 GAO20240513t163124p0000-E

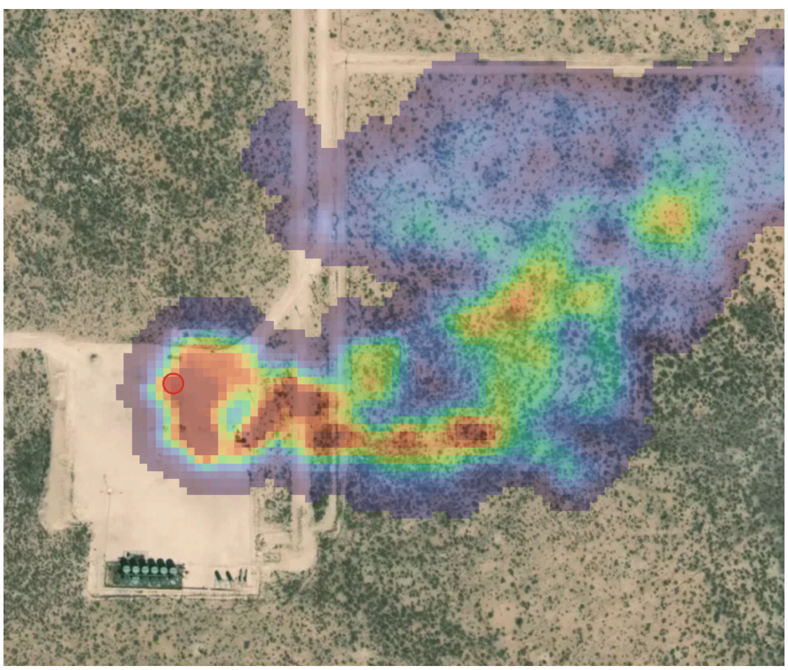

Figure S2.5.3 GAO20240517t152741p0000-J

S2.6. Other Gas Plant

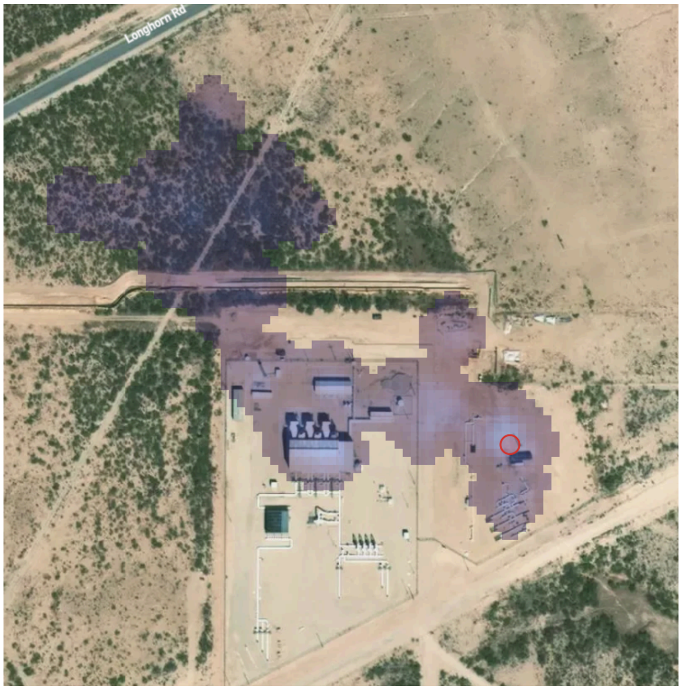

Figure S2.6.1 GAO20240501t193128p0000-C

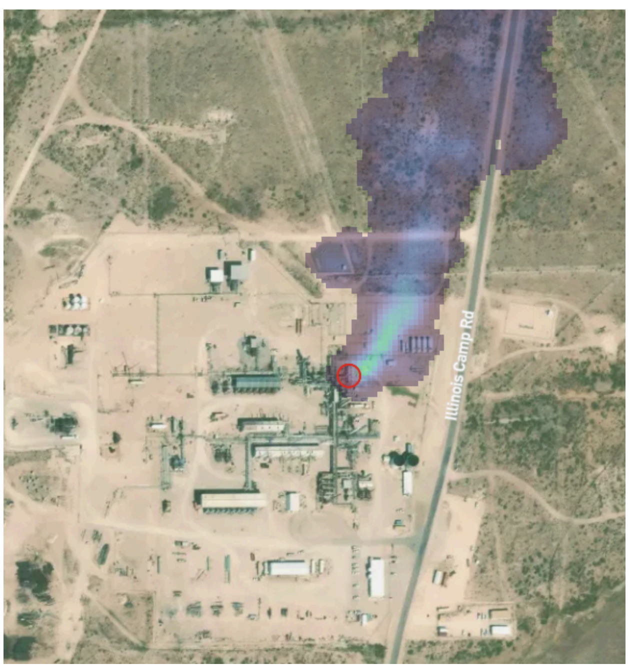

Figure S2.6.2 GAO20240501t193128p0000-C

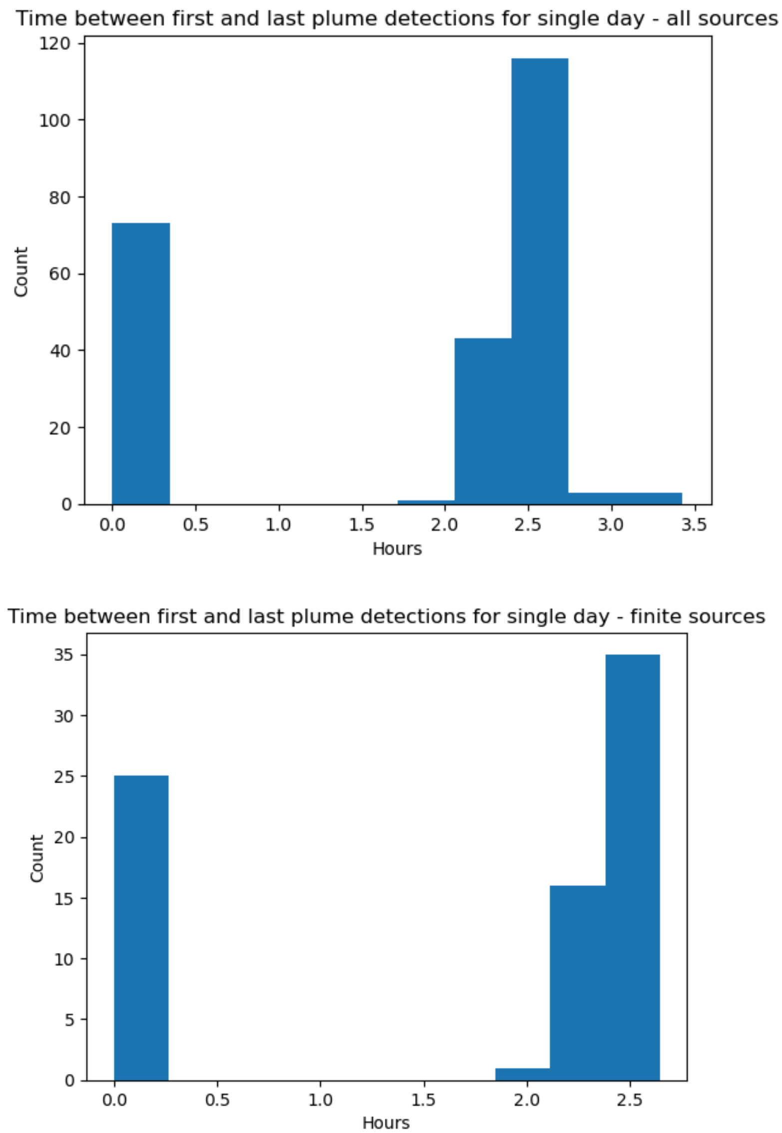

Figure S2. Distribution of elapsed time between first and last plume detections for sources that were sampled multiple times per day and where there was at least 2 hour spacing between the first and last observation at that source during that day.